Research Square

Preprints are preliminary reports that have not undergone peer review.
They should not be considered conclusive, used to inform clinical practice,
or referenced by the media as validated information.

Preparation and Electrochemical Performance Study of Covalent Organic Framework-Derived Porous Carbon@FeS2

Jie Chen
Lanzhou University of Technology
Peiting Miao
Lanzhou University of Technology
Jingyi Wang
Lanzhou University of Technology
Ying Wang
Lanzhou University of Technology
Jianqiang Zhang
Lanzhou University of Technology
Heming Luo
luohm666@163.com
Lanzhou University of Technology

Research Article

Keywords: FeS_2, COF-derived porous carbon, carbon framework, electrode composite, asymmetric supercapacito

Posted Date: November 12th, 2026

DOI: https://doi.org/10.21203/rs.3.rs-10684318/v1

License: This work is licensed under a Creative Commons Attribution 4.0 International License.
Read Full License

Additional Declarations: No competing interests reported.

Preparation and Electrochemical Performance Study of Covalent Organic Framework-Derived Porous Carbon@FeS_2

Jie Chen, Peiting Miao, Jingyi Wang, Ying Wang, Jianqiang Zhang*, Heming Luo*

School of Petrochemical Technology, Lanzhou University of Technology, Lanzhou 730050, China

* Corresponding author. E-mail address: zhangjq@lut.edu.cn (J Zhang), luohm666@163.com (H Luo).
School of Petrochemical Technology, Lanzhou University of Technology, Lanzhou 730050, China

Abstract

Covalent organic frameworks (COFs) offer designable skeletons and ordered pore domains, but poor charge transport and insufficient electrochemically active sites hinder their direct use as electrodes. In this work, COF-Bq was first obtained by Knoevenagel condensation and then transformed by carbonization and KOH activation into COF-BqC-700-3. A hydrothermal step grew FeS_2 within and on this porous carbon, giving COF-BqC-700-3@FeS_2 composites. The optimized COF-BqC-700-3@FeS_2-160-2 maintained hierarchical porosity dominated by micropores and reached 740.2 F g^{-1} at 1 A g^{-1}. When assembled with COF-BqC-700-3 in an asymmetric device, it delivered 25.03 Wh kg^{-1} at 750 W kg^{-1}. The device retained 90.95% capacitance after 5,000 cycles and showed 99.93% Coulombic efficiency. These results show that FeS_2 adds Faradaic storage sites to COF-derived carbon while the porous carbon framework supports charge transfer and ion transport.

Keywords: FeS_2; COF-derived porous carbon; carbon framework; electrode composite; asymmetric supercapacito.

1 Introduction

Electrical grids with a growing share of renewable power require storage systems that can respond rapidly to fluctuating supply[1]. Supercapacitors are well suited to this role because they provide fast charge-discharge behavior and long cycling durability[2]. Carbon-based electrodes are widely used in these devices, as their porous networks can expose a large interfacial area and support electron transport[3]. Their main limitation is that purely double-layer storage usually gives modest energy density when few redox-active sites are present[4]. A practical route to higher capacitance is therefore to couple conductive carbon frameworks with transition-metal compounds that can provide reversible Faradaic reactions.

FeS_2 is a promising metal sulfide component for hybrid supercapacitor electrodes because the Fe/S redox couple can participate in charge storage[5, 6]. The material is also inexpensive, earth-abundant and relatively benign, which is important for scalable energy-storage materials[7]. Sengodan et al.[8] reported a petal-like FeS_2/r-GO electrode prepared by hydrothermal synthesis, obtaining 748 F g^{-1} at 0.5 A g^{-1} and 31.18 Wh kg^{-1} at 10,512 W kg^{-1} for the FeS_2/r-GO//AC device. These results show the benefit of combining FeS_2 with carbon, while also highlighting the need to control FeS_2 placement and preserve open ion-transport pathways.

In this study, COF-derived porous carbon was selected as the host matrix for FeS_2. COF-Bq was synthesized through Knoevenagel condensation, carbonized and KOH-activated to produce COF-BqC-700-3. FeS_2 was then introduced by hydrothermal growth so that the sulfide phase formed on the carbon surface and within accessible pores. This architecture was designed to reduce FeS_2 aggregation while retaining conductive and porous channels. The effects of hydrothermal temperature and FeS_2 loading were evaluated, and the optimized composite was tested as the positive electrode in an asymmetric supercapacitor.

2 Experimental Procedures

2.1 Chemicals and Equipment

The analytical methods and corresponding instruments are summarized below to make the characterization conditions explicit.Table S1 lists all characterization instruments, models and manufacturers used throughout this work.

Table S1. Instruments used for structural, textural and electrochemical characterization.

Analysis or test	Instrument/model	Supplier
FT-IR spectroscopy	Nicolet Is 10	Thermo Fisher Scientific,USA
Powder X-ray diffraction	Bruker D8 Advance	Bruker AXS,Germany
Thermogravimetric analysis	Netzsch STA 2500	Netzsch Scientific Instruments,China
Raman spectroscopy	Horiba LabRAM HR Evolution	Shanghai Juna Technology Co.,Ltd.,China
X-ray photoelectron spectroscopy	Thermo Fisher Scientific system	Thermo Fisher Scientific,USA
Scanning electron microscopy	JSM-6701F	Shanghai Baihe Instrument Technology Co.,Ltd.,China
Transmission electron microscopy	FEI Titan G2 60-300	FEI Company,USA
N_2adsorption-desorption	Quantachrome Nova 4000e	Quantachrome Instruments,USA
Electrochemical workstation	CHI660D	CH Instruments,China
Battery testing	CT2001A	LAND Electronics Co.,Ltd.,China

The chemicals and electrode materials were used without further purification unless otherwise stated. All raw chemical reagents and commercial electrode substrates applied in synthesis and electrode fabrication are summarized in Table S2.

Table S2. Chemicals and electrode materials used in this work.

Supplier	Materials
Macklin Biochemical Co., Ltd.	1,4-Benzoquinone; 4-aminobenzonitrile; BTCA; sodium tert-butoxide; iron acetylacetonate; zinc chloride
Sinopharm Chemical Reagent Co., Ltd.	Methanol; ethanol; diethyl ether; KOH; HCl; acetone
Suzhou Yilongsheng Technology Co., Ltd.	Nickel foam; acetylene black; PTFE
Grade/use note	Analytical-grade reagents were used as received unless a separate pretreatment is specified.

2.2 Synthesis of Bq and COF-Bq

To synthesize Bq, the two monomers were handled as separate ethanol solutions before coupling. 4-Aminobenzyl cyanide (10 mmol) was dissolved in 20 mL anhydrous ethanol, and p-benzoquinone (15 mmol) was dissolved in another 20 mL portion of the same solvent. The two solutions were then mixed and kept at 60 °C for 18 h. The dark-red product was collected by filtration, rinsed with ethanol followed by diethyl ether, and dried in vacuo at 80 °C for 24 h. The obtained 2,5-bis-(4-aminobenzyl cyanide)-p-benzoquinone intermediate was denoted as Bq.

For COF-Bq formation, Bq (1.5 mmol) and BTCA (1.1 mmol) were suspended in 45 mL ethanol, followed by sodium tert-butoxide (3 mmol) as the base. The reaction was conducted under N_2 at 100 °C for 3 h. After cooling, the solid framework was isolated and washed in the order of ethanol, diethyl ether and deionized water. The cleaned precipitate was dried at 80 °C for 10 h, yielding brown COF-Bq powder[9].

2.3 Carbonization and KOH Activation of COF-Bq

COF-BqC-700 was produced through Ar-protected pyrolysis. COF-Bq powder was loaded in a porcelain boat and introduced into a tube furnace. The furnace was programmed to reach 700 °C at 5 °C min^{-1}, held at this temperature for 2 h, and then

cooled to room temperature under Ar. The notation COF-BqC-700 refers to the carbon material obtained from COF-Bq at 700 °C.

Chemical activation was then performed with KOH. COF-BqC-700 was physically mixed with KOH at a carbon-to-alkali mass ratio of 1:3 and treated at 700 °C under Ar for 2 h using a 5 °C min^{-1} heating rate. The cooled solid was washed with 1 M HCl and deionized water to eliminate inorganic residues. After drying, the final activated carbon was labeled COF-BqC-700-3.

2.4 Hydrothermal Synthesis of COF-BqC-700-3@FeS_2-T-a

The COF-BqC-700-3@FeS_2-T-a series was prepared through an aqueous hydrothermal route. Polyvinylpyrrolidone (0.2 g) was dissolved in 20 mL pure water, while COF-BqC-700-3 (0.05 g) was dispersed ultrasonically in another 20 mL portion of pure water. After combining the two liquids, $FeSO_4·7H_2O$ (0.4, 0.8 or 1.2 mmol) and $Na_2S_2O_3·5H_2O$ were added, with the amount of $Na_2S_2O_3·5H_2O$ set at twice the molar amount of $FeSO_4·7H_2O$. The suspension was stirred for 30 min, transferred to an autoclave, and heated at 140, 160 or 180 °C for 24 h. The obtained powder was washed with deionized water and anhydrous ethanol before vacuum drying at 80 °C for 12 h. The product notation COF-BqC-700-3@FeS_2-T-a uses T for the hydrothermal temperature and a for the mass ratio of COF-derived carbon to FeS_2. Bare FeS_2 was synthesized by the same 160 °C procedure using 0.8 mmol $FeSO_4·7H_2O$ and 1.6 mmol $Na_2S_2O_3·5H_2O$, but without COF-BqC-700-3.The synthetic route for COF-BqC-700-3@FeS_2-T-a composite is schematically illustrated in Figure 1.

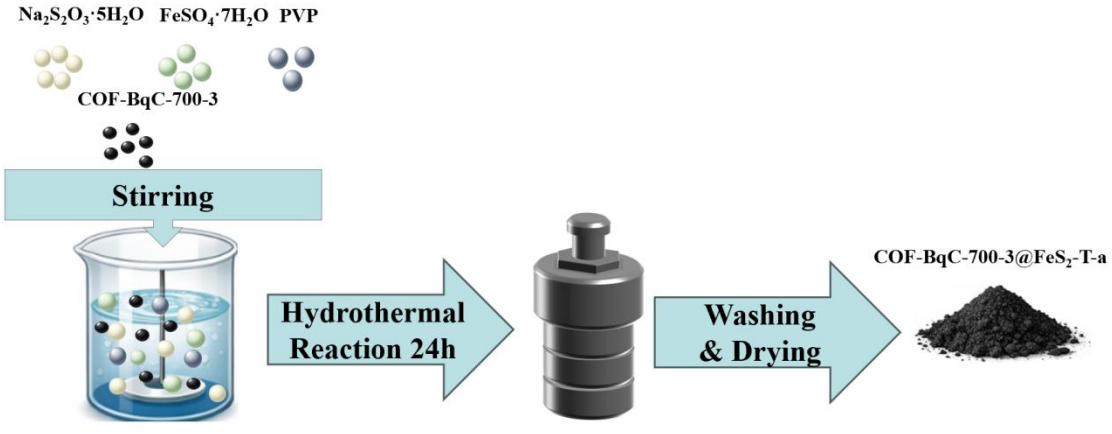


Figure 1 Synthesis schematic of COF-BqC-700-3@FeS_2-T-a

2.5 Electrochemical Measurements

2.5.1 Electrode Fabrication and Asymmetric Device Assembly

Before slurry coating, nickel foam was cleaned by sequential ultrasonication in 3 M HCl, acetone and ultrapure water, and was then dried under vacuum at 60 °C. The active electrode material, acetylene black and PTFE emulsion were combined at a mass ratio of 16:3:1. A small amount of anhydrous ethanol was used to wet and disperse the mixture, which was manually ground into a cohesive paste. The paste was applied to a 1 × 1 cm^2 area of the pretreated nickel foam, dried at 60 °C, and pressed at 12 MPa for 1.5 min.

The asymmetric device used COF-BqC-700-3@FeS_2-160-2 as the positive electrode and COF-BqC-700-3 as the negative electrode. Circular nickel foam was used as the current collector. Before assembly, both electrodes were immersed in 6 M KOH for 10 min. A separator was then placed between the two opposing electrodes to complete the cell.

2.5.2 Equations Used for Electrochemical Calculations

Electrochemical measurements were conducted in 6 M KOH. In the three-electrode setup, COF-BqC-700-3@FeS_2-T-a served as the working electrode, Hg/HgO as the reference electrode, and a platinum plate as the counter electrode. CV, GCD and EIS data were collected within a potential window of 0 to −0.45 V.

The capacitance from three-electrode GCD profiles was obtained from the discharge branch according to Eq. (1)[10]:

$$C = \frac{I\Delta t}{m\Delta V} \tag{1}$$

This calculation normalizes the discharge response by the mass of active material and the applied potential window.

The dependence of peak current on scan rate was analyzed with the power-law fit in Eq. (2)[11]:

$$log(i) = blog(v) + log(a) \tag{2}$$

The resulting b value was used to assess whether the current response was closer

to diffusion-controlled or surface-controlled behavior.

For the assembled two-electrode cell, gravimetric energy density and power density were calculated from Eqs. (3) and (4)[12]:

$$E = \frac{\frac{1}{2C\Delta V^2} \times 1000}{3600} \tag{3}$$

$$P = \frac{E \times 3600}{\Delta t} \tag{4}$$

The discharge duration used for the power-density calculation was taken from the corresponding GCD curve.

The capacitive and diffusion-related current contributions were separated using Eq. (5)[13]:

$$i = k_1 v + k_2 v^{\frac{1}{2}} \tag{5}$$

In this expression, the term proportional to scan rate describes the surface-controlled contribution, whereas the square-root term describes the diffusion-governed contribution.

The mass ratio of the two electrodes in the asymmetric cell was selected from the charge-balance relation in Eq. (6)[14]:

$$\frac{m_+}{m_-} = \frac{C_{m-}V_-}{C_{m+}V_+} \tag{6}$$

All mathematical symbols, physical meanings and corresponding units applied in Eqs. (1)–(6) are defined in Table S3 for better readability.

Table S3. Definition of variables used in electrochemical calculations.

Symbol	Definition	Unit or role
C	Specific capacitance or cell capacitance used in the relevant calculation	F g^{-1}
I	Discharge current used for the GCD-derived capacitance calculation	A
Δt	Discharge time read from the GCD curve	s
ΔV	Potential or voltage window used for the corresponding measurement	V
m	Mass term used for capacitance or charge-balance normalization	g or mg
i	Peak current used in kinetic fitting	A or A g^{-1}
v	CV scan rate	mV s^{-1}
a,b	Fitted constants in the power-law relationship	dimensionless or fitted coefficient
E,P	Energy density and power density of the assembled cell	Wh kg^{-1};W kg^{-1}
k_1,k_2	Coefficients for surface-controlled and diffusion-governed current terms	fitting parameters
+,−	Positive and negative electrodes in the asymmetric device	electrode label

3 Results and Discussion

3.1 Structure Analysis of COF-Bq

Figure 2 gives the FTIR and XRD characterization of COF-Bq. In Figure 2(a), Bq and COF-Bq both display the –C≡N band at 2247 cm^{-1}[15]. After framework formation, the C–H bands at 3062 and 2871 cm^{-1} are no longer visible, and the aldehyde C=O band at 1697 cm^{-1} also disappears. This result indicates that BTCA participated in the condensation reaction. The band at 3223 cm^{-1} is attributed to residual N–H stretching, while the 1570 cm^{-1} band is assigned to the C=C vibration in C=C–C≡N[15]. The XRD pattern in Figure 2(b) shows reflections at 2θ = 14.3°, 17.8°, 19.2°, and 25.6°. The 25.6° reflection is related to aromatic-layer π–π stacking and indicates ordered layer

packing[16]. These results confirm formation of crystalline COF-Bq.

The thermal response of COF-Bq was evaluated by TGA-DTG (Figure 2(c)). A 1.64% mass decrease below 202 °C is mainly related to removal of physically adsorbed water and residual solvent. The 6.83% decrease at 357.0 °C corresponds to decomposition of chain segments and heteroatom-containing groups such as C–O and C≡N. When the temperature reaches 1000 °C, the total mass loss increases to 35.71%. This process involves destruction of the COF-Bq framework, evolution of CO_2 and water vapor, and conversion of carbon fragments into graphitized amorphous carbon. The maximum DTG signal at 357 °C marks the main decomposition process.

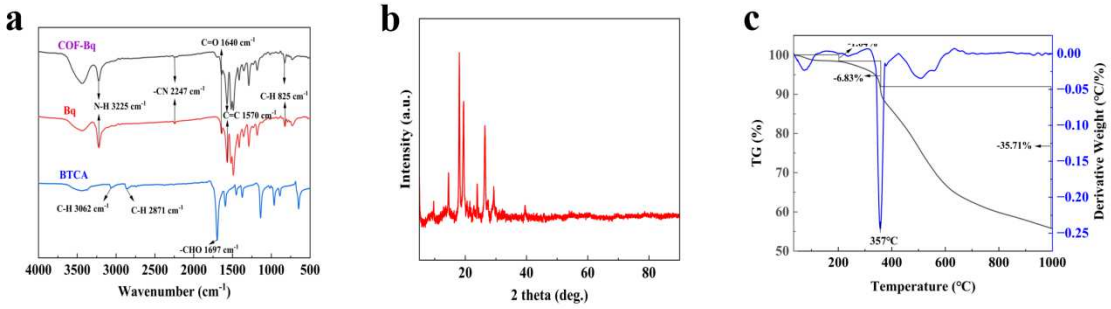


Figure 2. (a) FTIR spectrum, (b) XRD pattern, and (c) TGA-DTG curves of COF-Bq.

3.2 Phase Analysis of FeS_2 and COF-BqC-700-3@FeS_2-160-2

Figure 3 compares the XRD patterns of FeS_2 and COF-BqC-700-3@FeS_2-160-2. Diffraction peaks of FeS_2 occur at $2\theta \approx 28.5°$, 33.1°, 37.1°, 40.8°, 47.4°, 56.2°, 59.0°, 61.6°, and 64.2°. These peaks are indexed to the (111), (200), (210), (211), (220), (311), (222), (023), and (321) planes of pyrite FeS_2 (PDF#97-063-3293)[17]. The peak set verifies the presence of FeS_2 in the composite. A broad signal around $2\theta \approx 25°$ is attributed to the (002) plane of COF-derived carbon, indicating an amorphous carbon structure.The weak (100) graphitic-carbon feature further suggests limited graphitization[18].

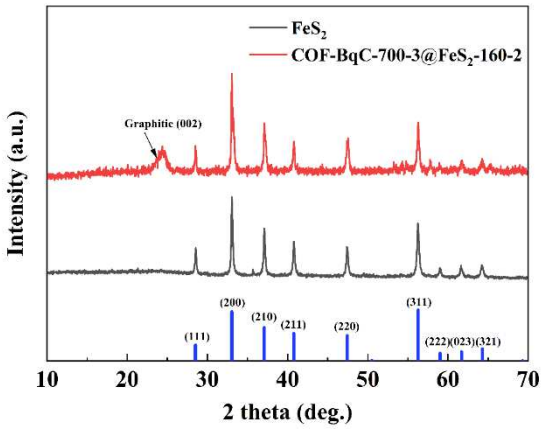


Figure 3. XRD patterns of COF-BqC-700-3@FeS_2-160-2 and FeS_2

3.3 Morphology of COF-BqC-700-3@FeS_2-160-2

Figure 4 presents the morphology and elemental distribution. The FeS_2 reference sample consists of flower-like microspheres assembled from radially oriented sheets (Figure 4(a)). For the composite, SEM and TEM images (Figure 4(b)) show FeS_2 distributed on the porous carbon skeleton and inside accessible channels. In Figure 4(c), dark contrast corresponds to FeS_2 particles, while the lighter region corresponds to the carbon matrix. This contrast verifies contact between FeS_2 and the carbon host. The 0.192 nm lattice spacing in Figures 4(d) and 4(e) is indexed to the FeS_2 (220) plane (PDF#97-063-3293), in agreement with the XRD result. EDS mapping in Figure 4(f) gives C, O, Fe, and S contents of 64.56%, 5.11%, 7.95%, and 21.46%, respectively, confirming FeS_2 distribution in the carbon framework.

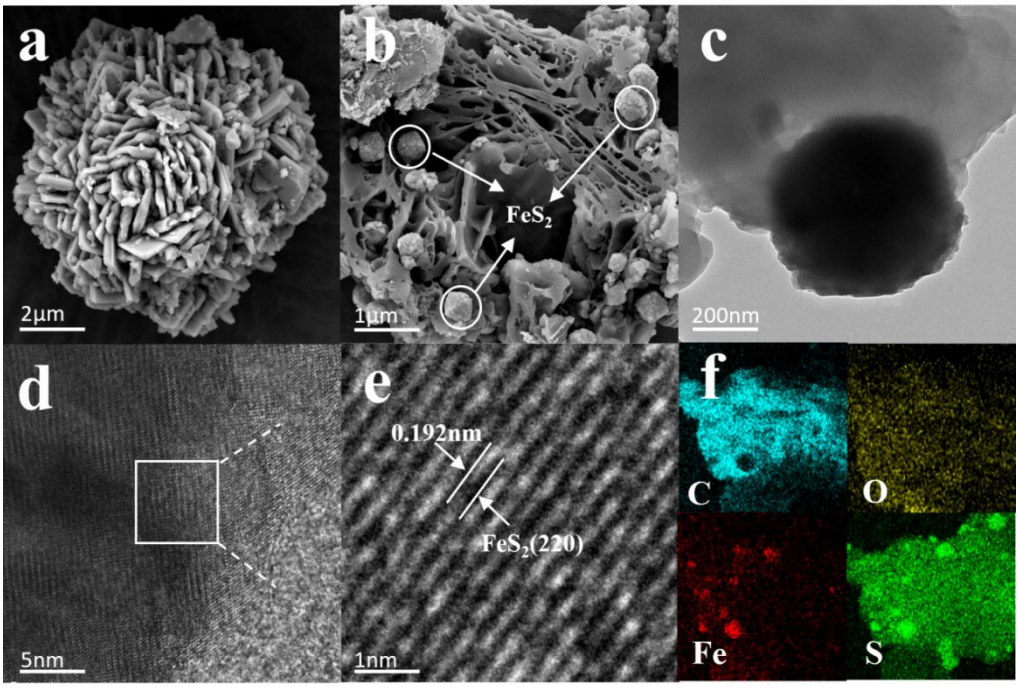


Figure 4. Microscopy and EDS mapping of bare FeS_2 and COF-BqC-700-3@FeS_2-160-2 composite. (a) SEM image of pristine FeS_2. (b) SEM image of COF-BqC-700-3@FeS_2-160-2 composite. (c) TEM micrograph of the composite. (d, e) HRTEM images showing the lattice fringe of the FeS_2 (220) plane. (f) Corresponding EDS elemental mappings of C, O, Fe and S for COF-BqC-700-3@FeS_2-160-2.

3.4 Surface Chemical States of COF-BqC-700-3@FeS_2-160-2

Figure 5 presents the surface chemistry of COF-BqC-700-3@FeS_2-160-2 was examined by XPS. The survey scan confirms the presence of C, N, O, Fe and S. The C, N and O signals are associated with the COF-derived carbon matrix, while Fe and S arise from the FeS_2 phase. In the C 1s spectrum, the components at 284.8, 286.1 and 288.4 eV are assigned to C=C/C–C, C–O and C=O bonding environments, respectively[19]. The Fe 2p profile shows Fe^{2+} $2p_{3/2}$ and Fe^{2+} $2p_{1/2}$ features at 707.0 and 719.8 eV, consistent with pyrite FeS_2. The S 2p spectrum contains sulfide-sulfur maxima at 162.2 and 163.6 eV. The signal at 168.7 eV is related to oxidized sulfur, most likely from sulfate residues or slight surface oxidation[20]. For N 1s, the fitted peaks at 398.3, 399.6 and 400.3 eV indicate pyridinic, pyrrolic and graphitic nitrogen, respectively[21]. The O 1s signals at 531.8 and 533.4 eV are in relation with C=O and C–O groups[22]. Together, these spectra verify the coexistence of FeS_2 and oxygen-containing carbon species in the composite.

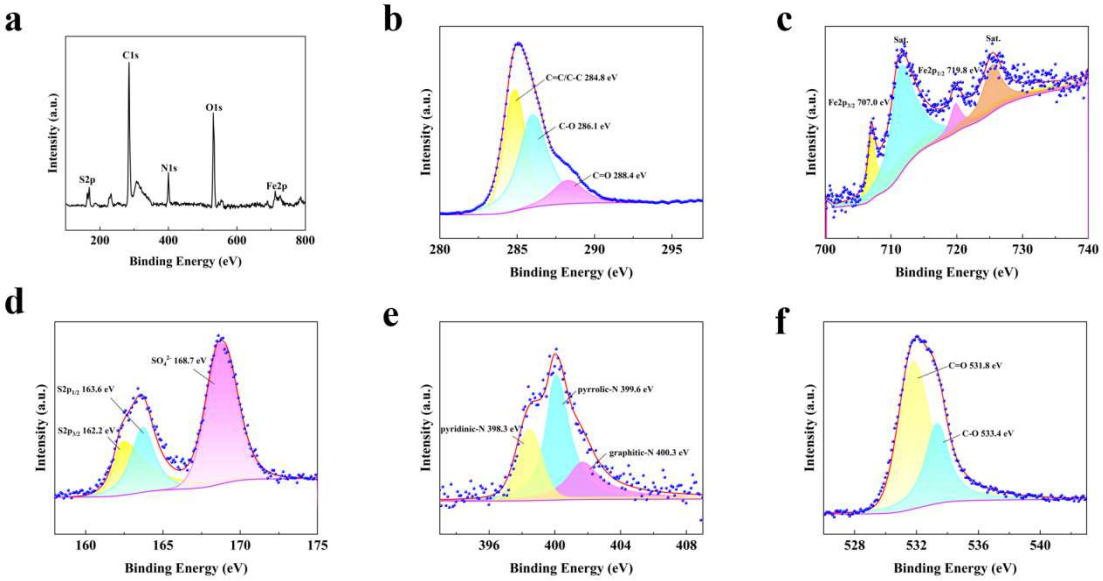


Figure 5. XPS survey spectrum and high-resolution core-level XPS spectra of COF-BqC-700-3@FeS_2-160-2 composite. (a) XPS survey spectrum; (b) high-resolution C 1s spectrum; (c) high-resolution Fe 2p spectrum; (d) high-resolution S 2p spectrum; (e) high-resolution N 1s spectrum; (f) high-resolution O 1s spectrum.

3.5 Nitrogen Adsorption-Desorption Analysis

Figure 6 compares the pore structure of the adsorption and desorption of Nitrogen. FeS_2 shows negligible N_2 uptake across the tested relative-pressure range, showing limited porosity and a very small surface area. The COF-BqC-700-3@FeS_2-160-a composites show combined type-I and type-IV isotherm characteristics under IUPAC classification. Rapid uptake at $p/p_0 < 0.01$ is associated with micropore filling, and the H4 hysteresis loop within $0.4 < p/p_0 < 0.9$ indicates mesopores. The uptake at $p/p_0 > 0.9$ reflects the presence of larger pores[23]. Figure 6(b) shows broad macropore-related voids in FeS_2, probably from spaces among stacked FeS_2 particles. The composites mainly show pores of 1–3 nm, which can provide electrolyte-ion storage sites and transport channels.

Table 1 summarizes the textural parameters. The SBET values of COF-BqC-700-3 and COF-BqC-700-3@FeS_2-160-a are 1900.98, 349.53, 327.79, and 189.25 $m^2\ g^{-1}$, respectively. Their micropore ratios are 95.30%, 84.33%, 94.08%, and 86.28%. The decrease in surface area with increasing FeS_2 loading indicates that FeS_2 partly covers

carbon surfaces and occupies pore space. The high micropore ratio of COF-BqC-700-3@FeS_2-160-2 favors electric double-layer charge storage. FeS_2 also supplies redox-active sites. Thus, the composite integrates carbon-based double-layer capacitance with FeS_2-derived pseudocapacitance.

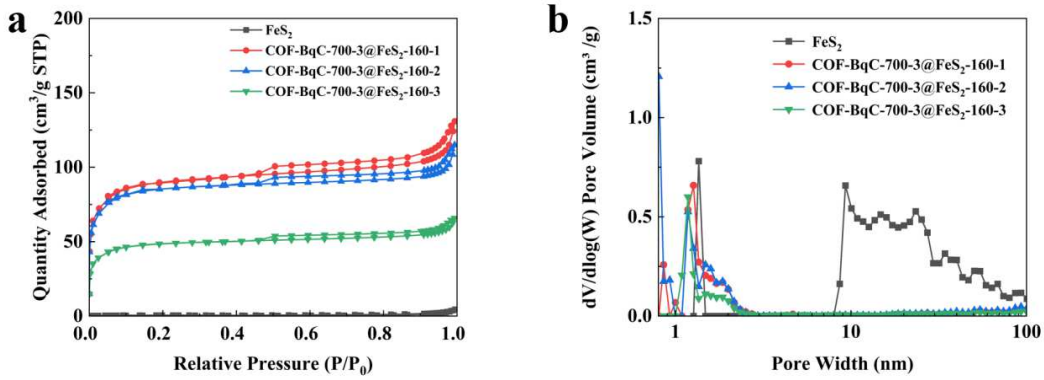


Figure 6. Comparison between the nitrogen ad-desorption isotherms and pore size in FeS_2 & COF-BqC-700-3@FeS_2-160-a.

Table 1 Porosity and surface-area data for FeS_2 and COF-BqC-700-3@FeS_2-160-a.

Sample	S_{BET} /(m^2 g^{-1})	S_{micro} /(m^2 g^{-1})	S_{micro} /S_{BET}/(%)	V_{total} /(cm^3 g^{-1})	$D_{average}$ /nm
FeS_2	1.84	0.98	53.26	0.01	14.98
COF-BqC-700-3@FeS_2-160-1	349.53	294.78	84.33	0.20	2.31
COF-BqC-700-3@FeS_2-160-2	327.79	308.40	94.08	0.18	2.17
COF-BqC-700-3@FeS_2-160-3	189.25	163.28	86.28	0.10	2.15
COF-BqC-700-3	1900.98	1811.72	95.30	0.84	1.76

3.6 Electrochemical Properties and Charge-Storage Behavior

3.6.1 Effect of Synthesis Conditions on Electrochemical Behavior

Figure 7 compares the electrochemical behavior of samples prepared with different hydrothermal temperatures and FeS_2 loadings. Figure 7(a) shows GCD curves of COF-BqC-700-3@FeS_2-T-2 at 1.0 A g^{-1}. The discharge plateaus indicate reversible Faradaic reactions and pseudocapacitive behavior[24]. According to Equation (1), the capacitances are 573.7, 740.2, and 615.5 F g^{-1}. The 160 °C sample gives the best

performance, which is consistent with suitable FeS_2 formation. Lower temperature limits FeS_2 growth, whereas excessive temperature can promote aggregation and pore blocking, slowing ion transport. The CV curves in Figure 7(b) show redox peaks, confirming coupled double-layer and pseudocapacitive charge storage[25]. COF-BqC-700-3@FeS_2-160-2 gives the largest CV area, agreeing with the GCD result. Figure 7(c) compares samples with different FeS_2 amounts at 1.0 A g^{-1}. The relevant capacitances present the value of 652.4, 740.2, and 688.1 F g^{-1}. A moderate FeS_2 content increases redox sites, whereas excessive loading reduces accessible area and active-site utilization. The capacitance of COF-BqC-700-3@FeS_2-160-2 is higher than those reported for FeS_2@Carbon (278.4 F g^{-1} at 1 A g^{-1})[26], FeS_2-CNFs (511 F g^{-1} at 1 A g^{-1})[27], and FeS_2-SRGO (277 F g^{-1} at 1 A g^{-1})[28]. The CV areas in Figures 7(b) and 7(d) show the same trend.

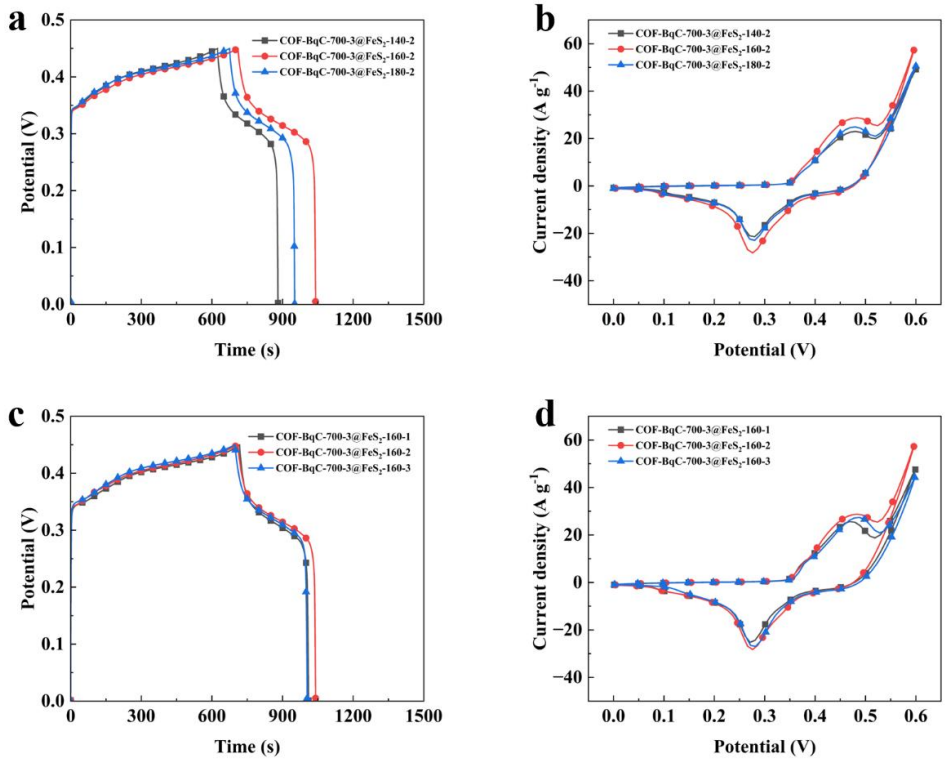


Figure 7. GCD and CV responses of COF-BqC-700-3@FeS_2-T-2 and COF-BqC-700-3@FeS_2-160-a.

3.6.2 Electrochemical Response of COF-BqC-700-3@FeS_2-160-2

Figures 8(a–c) compare COF-BqC-700-3@FeS_2-160-2 with FeS_2 and COF-BqC-700-3. COF-BqC-700-3 exhibits an approximately triangular GCD curve, indicating

electric double-layer storage. FeS_2 and COF-BqC-700-3@FeS_2-160-2 display discharge plateaus, indicating pseudocapacitive reactions[29]. Bare FeS_2 shows lower capacitance because of its limited surface area and conductivity. At 1.0 A g^{-1}, the capacitances of the composite, FeS_2, and COF-BqC-700-3 are 740.2, 495.4, and 351.9 F g^{-1}, respectively. The composite value reflects the combined role of porous carbon and FeS_2. In Figure 8(b), FeS_2-containing electrodes show redox peaks at 10 mV s^{-1}[30], whereas COF-BqC-700-3 keeps a nearly rectangular CV shape. When current density increases from 1 to 10 A g^{-1}, the capacitance retentions are 64.7%, 34.9%, and 82.6%, respectively. The carbon framework supports charge transport, while FeS_2 provides redox activity.

Figures 8(d–f) analyze the charge-storage kinetics of COF-BqC-700-3@FeS_2-160-2. The CV curves maintain similar profiles from 10 to 100 mV s^{-1}, indicating reversible electrode behavior. In Figure 8(e), peak current is plotted as a function of scan rate. Equation (2) gives b-values of 0.630 for the cathodic peak and 0.551 for the anodic peak. Because both values are between 0.5 and 1.0, diffusion-controlled and surface-controlled processes both contribute to the response, consistent with hybrid capacitance[8]. Figure 8(f) shows the capacitive fraction. At 10 mV s^{-1}, Equation (5) gives a 19.35% surface-controlled contribution, indicating diffusion-dominated storage at low scan rate. At 100 mV s^{-1}, this contribution increases to 45.34%, showing greater participation of surface adsorption/desorption. These results reflect the combined effects of porous-carbon transport pathways and FeS_2 redox sites.

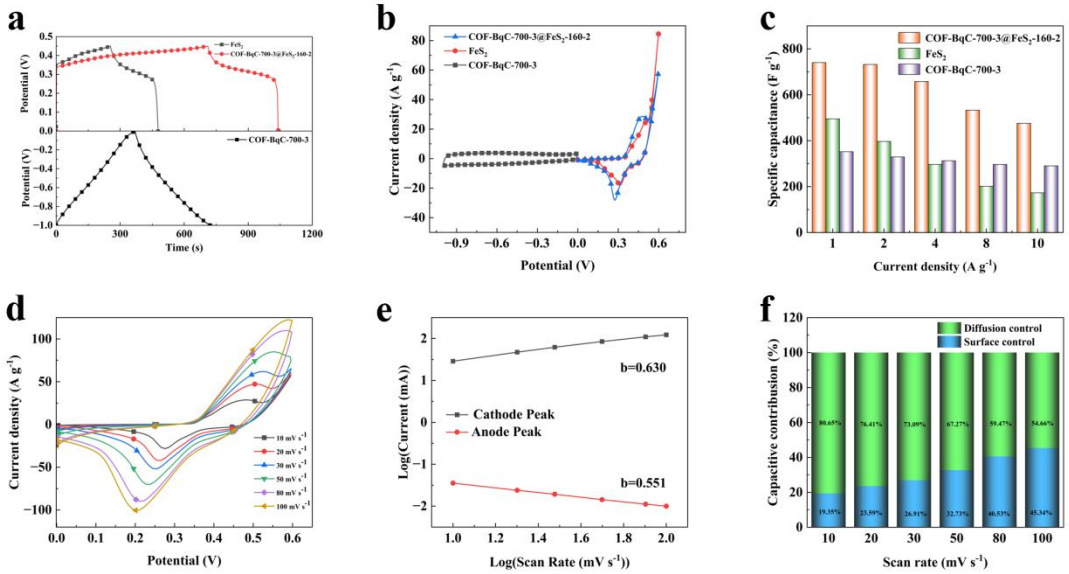


Figure 8. (a) galvanostatic charge–discharge (GCD) curves at 1.0 A g^{-1}; (b) cyclic voltammetry (CV) curves at 10 mV s^{-1}; (c) specific capacitances at different current densities; (d) CV curves at different scan rates; (e) linear relationship between scan rate and anodic/cathodic peak currents; (f) capacitive contribution ratios at different scan rates.

3.7 Performance of the Assembled Asymmetric HSC

The COF-BqC-700-3@FeS_2-160-2//COF-BqC-700-3 asymmetric HSC was assembled to evaluate device-level performance. COF-BqC-700-3@FeS_2-160-2 was used as the positive electrode, and COF-BqC-700-3 was used as the negative electrode in 6 M KOH. Figure 9(a) shows curved GCD profiles, indicating combined electric double-layer and Faradaic storage. The current density increases (1-10 A g^{-1}) while the capacitance exhibit opposite trends (80.1-50.3 F g^{-1}) , corresponding to 62.8% retention. Equations (3) and (4) give an energy density of 25.03 Wh kg^{-1} at a power density of 750 W kg^{-1}. The CV curves in Figure 9(b) retain similar shapes at different scan rates, indicating stable reversibility and rate response. After 5,000 cycles at 2.0 A g^{-1}, the cell retains 90.95% capacitance and shows 99.93% Coulombic efficiency, indicating stable operation.

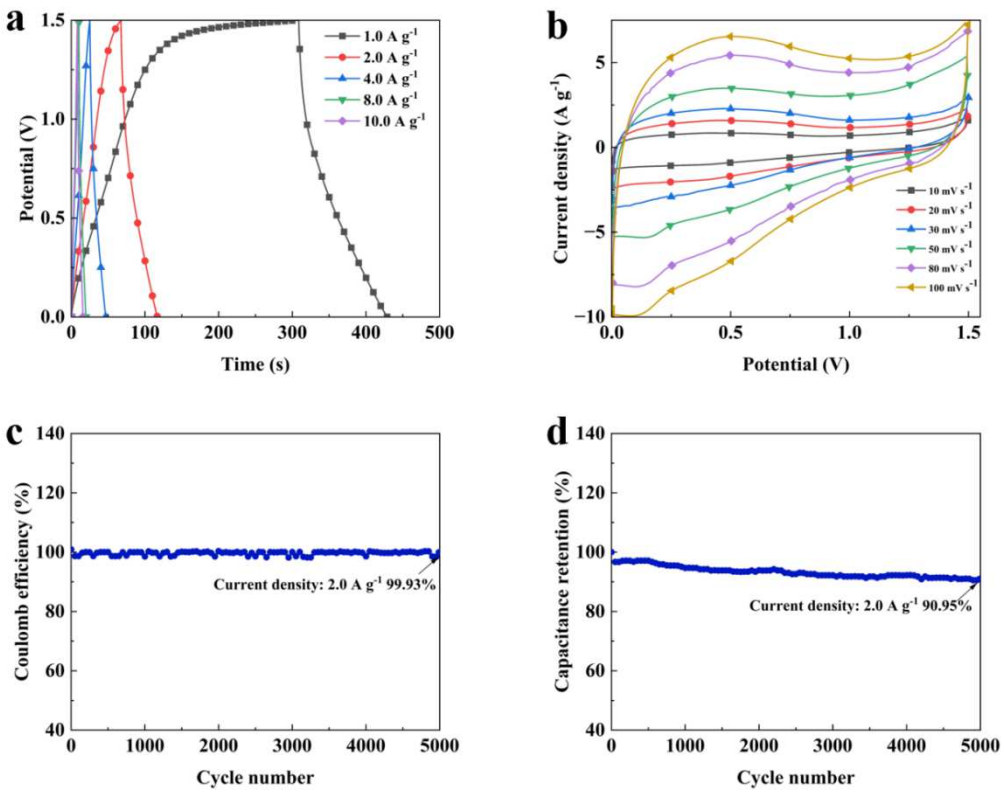


Figure 9. Performance of the asymmetric HSC: GCD behavior, CV response, capacitance retention, and Coulombic efficiency.

4 Conclusions

This work prepared COF-BqC-700-3@FeS_2-160-2 by converting COF-Bq into KOH-activated porous carbon and subsequently introducing FeS_2 through hydrothermal growth. The optimized composite delivered 740.2 F g^{-1} at 1.0 A g^{-1}. When paired with COF-BqC-700-3 in an asymmetric HSC, the device provided 80.1 F g^{-1} and an energy density of 25.03 Wh kg^{-1} at 750 W kg^{-1}, which exceeded the symmetric porous-carbon device value of 12.13 Wh kg^{-1}. The cell retained 90.95% of its capacitance after 5,000 cycles and maintained 99.93% Coulombic efficiency. These results support an electrode design in which FeS_2 supplies redox-active sites and the COF-derived carbon framework preserves conductive, ion-accessible pores.

Author Contributions

Jie Chen: Conceptualization, Investigation, Methodology, Writing-original draft.

Peiting Miao: Formal analysis, Writing-review & editing. Jingyi Wang: Formal analysis. Ying Wang:Writing-review. Jianqiang Zhang: Conceptualization, Investigation, Supervision, Writing-review & editing. Heming Luo: Conceptualization, Methodology, Resources, Funding acquisition, Validation, Supervision, Writing-review & editing.

Data Availability Statement

Data will be made available on request.

Conflicts of Interest

The authors declare that they have no known competing financial interests or personal relationships that could have influenced the work reported in this paper.

Funding Declaration

This work was supported by the National Natural Science Foundation of China (Grant No. 22166023), the Industrial Support Plan Project of Colleges and Universities in Gansu Province (Grant No. 2023CYZC-30), the Talents Innovation and Entrepreneurship Project of Lanzhou (Grant No. 2021-RC-20), and the National Key Research and Development Innovative methods work special Program of China (SQ2020IM030400).

References

[1] Gür, T. M. Review of electrical energy storage technologies, materials and systems: challenges and prospects for large-scale grid storage. *Energy & environmental science* **2018**, *11* (10), 2696-2767.

[2] Salanne, M.; Rotenberg, B.; Naoi, K.; Kaneko, K.; Taberna, P.-L.; Grey, C. P.; Dunn, B.; Simon, P. Efficient storage mechanisms for building better supercapacitors. *Nature Energy* **2016**, *1* (6), 1-10.

[3] Liu, H.; Liu, X.; Li, W.; Guo, X.; Wang, Y.; Wang, G.; Zhao, D. Porous carbon composites for next generation rechargeable lithium batteries. *Advanced Energy Materials* **2017**, *7* (24), 1700283.

[4] Li, Z.; Xu, K.; Pan, Y. Recent development of supercapacitor electrode based on carbon materials. *Nanotechnology Reviews* **2019**, *8* (1), 35-49.

[5] Li, X.; Qi, S. H.; Zhang, W. C.; Feng, Y. Z.; Ma, J. M. Recent progress on FeS2 as anodes for metal-ion batteries. *Rare Metals* **2020**, *39* (11), 1239-1255.

[6] Kaur, G.; Kaur, M.; Thakur, A.; Kumar, A. Recent progress on pyrite FeS2 nanomaterials for energy and environment applications: synthesis, properties and future prospects. *Journal of Cluster Science* **2020**, *31* (5), 899-937.

[7] Farhan, A.; Qayyum, W.; Fatima, U.; Nawaz, S.; Balčiūnaitė, A.; Kim, T. H.; Srivastava, V.; Vakros, J.; Frontistis, Z.; Boczkaj, G. Powering the future by iron sulfide type material (FexSy) based electrochemical materials for water splitting and energy storage applications: a review. *Small* **2024**, *20* (33), 2402015.

[8] Sengodan, P.; Yuanmeng, T.; Yang, X.; Xiaoxian, S.; Luong, J. H.; Ammasi, A.; Orooji, Y. Design and fabrication of 3D petal-like FeS2/r-GO nanocomposite as a high-performance electrode in hybrid supercapacitors. *Fuel* **2025**, *394*, 135114.

[9] Durgaryan, A.; Arakelyan, R.; Durgaryan, N. Synthesis of polymers containing polyaniline fragments linked by 1, 4-benzoquinone groups. *Russian Journal of General Chemistry* **2017**, *87* (1), 139-144.

[10] Park, O.-K.; Kim, N. H.; Lee, J. H. Single-step fabrication of surface morphology tuned iron oxide anchored highly porous carbon nanotube hybrid foam for a highly stable supercapacitor electrode. *Journal of Colloid and Interface Science* **2023**, *641*, 479-491.

[11] Lu, Y.; Liang, J.; Deng, S.; He, Q.; Deng, S.; Hu, Y.; Wang, D. Hypercrosslinked polymers enabled micropore-dominant N, S Co-Doped porous carbon for ultrafast electron/ion transport supercapacitors. *Nano Energy* **2019**, *65*, 103993.

[12] Halder, S.; Garg, S.; Chakraborty, C. Introducing non-conjugated ionic spacer in metallo-supramolecular polymer: Generation of nanofibers for high-performance electrochromic supercapacitor. *Chemical Engineering Journal* **2023**, *470*, 144361.

[13] Jiang, D.; Wei, C.-Y.; Zhu, Z.-Y.; Guan, X.-H.; Lu, M.; Zhang, X.-J.; Wang, G.-S. Synthesis of 3D flower-like hierarchical NiCo-LDH microspheres with boosted electrochemical performance for hybrid supercapacitors. *Inorganic Chemistry Frontiers* **2021**, *8* (19), 4324-4333.

[14] Chen, H.; Hu, L.; Chen, M.; Yan, Y.; Wu, L. Nickel- Cobalt Layered Double Hydroxide Nanosheets for High- performance Supercapacitor Electrode Materials. *Advanced Functional Materials* **2014**, *24* (7), 934-942.

[15] Navarro-Suárez, A. M.; Carretero-González, J.; Rojo, T.; Armand, M. Poly (quinone-amine)/nanocarbon composite electrodes with enhanced proton storage capacity. *Journal of Materials Chemistry A* **2017**, *5* (44), 23292-23298.

[16] Wang, Q.; Chen, L.; Li, Y.; Yang, J.; Yang, R.; Yang, X. Magnetic nanocomposite-based TpPa-NO2 covalent organic framework for the extraction of pyrethroid insecticides in water, vegetable, and fruit samples. *Food Analytical Methods* **2023**, *16* (1), 71-82.
[17] Song, H.; Wu, M.; Tang, X.; Liang, J.; Zhang, Y.; Xie, Y.; Tang, Q.; Qin, L.; Fan, X. Synthesis of Fe_3O_4/FeS_2 composites via MOF-templated sulfurization for high-performance hybrid supercapacitors. *Journal of Alloys and Compounds* **2025**, *1010*, 177658.
[18] Moseenkov, S.; Kuznetsov, V.; Zolotarev, N.; Kolesov, B.; Prosvirin, I.; Ishchenko, A.; Zavorin, A. Investigation of amorphous carbon in nanostructured carbon materials (a comparative study by TEM, XPS, Raman spectroscopy and XRD). *Materials* **2023**, *16* (3), 1112.
[19] Tian, W.; Zhang, H.; Sun, H.; Tade, M. O.; Wang, S. Template-free synthesis of N-doped carbon with pillared-layered pores as bifunctional materials for supercapacitor and environmental applications. *Carbon* **2017**, *118*, 98-105.
[20] Wang, C.; Niu, Y.; Jiang, J.; Chen, Y.; Tian, H.; Zhang, R.; Zhou, T.; Xia, J.; Pan, Y.; Wang, S. Hybrid thermoelectric battery electrode FeS2 study. *Nano Energy* **2018**, *45*, 432-438.
[21] Shang, Z.; An, X.; Zhang, H.; Shen, M.; Baker, F.; Liu, Y.; Liu, L.; Yang, J.; Cao, H.; Xu, Q.; et al. Houttuynia-derived nitrogen-doped hierarchically porous carbon for high-performance supercapacitor. *Carbon* **2020**, *161*, 62-70.
[22] Jayaramulu, K.; Dubal, D. P.; Nagar, B.; Ranc, V.; Tomanec, O.; Petr, M.; Datta, K. K. R.; Zboril, R.; Gómez-Romero, P.; Fischer, R. A. Ultrathin hierarchical porous carbon nanosheets for high-performance supercapacitors and redox electrolyte energy storage. *Advanced Materials* **2018**, *30* (15), 1705789.
[23] Yang, B.; Zhang, D.; Li, Y.; He, Y.; Li, Y.; Li, Z.; Wang, B.; Han, Z.; Wang, K. Locally graphitized biomass-derived porous carbon nanosheets with encapsulated Fe3O4 nanoparticles for supercapacitor applications. *Chemical Engineering Journal* **2024**, *479*, 147662.
[24] Andikaey, Z.; Ensafi, A. A.; Rezaei, B. Iron-doped cobalt copper phosphide/phosphate composite with 3D hierarchical flower-like structures as electrodes for hybrid supercapacitors. *Electrochimica Acta* **2021**, *393*, 139061.
[25] Song, X.; Tan, L.; Wang, X.; Zhu, L.; Yi, X.; Dong, Q. Synthesis of CoS@rGO composites with excellent electrochemical performance for supercapacitors. *Journal of Electroanalytical Chemistry* **2017**, *794*, 132-138.
[26] Liu, X.; Deng, W.; Liu, L.; Wang, Y.; Huang, C.; Wang, Z. Passion fruit-like microspheres of FeS 2 wrapped with carbon as an excellent fast charging material for supercapacitors. *New Journal of Chemistry* **2022**, *46* (23), 11212-11219.
[27] Huang, Y.; Zhao, H.; Bao, S.; Yin, Y.; Zhang, Y.; Lu, J. Hollow FeS2 nanospheres encapsulated in N/S co-doped carbon nanofibers as electrode material for electrochemical energy storage. *Journal of Alloys and Compounds* **2022**, *905*, 164184.
[28] Hassanpoor, S.; Tamri, E. FeS2/SRGO nanocomposite: Synthesis, characterization and comprehensive study of supercapacitor behavior in different electrolytes. *Journal of Alloys and Compounds* **2023**, *932*, 167711.
[29] Qin, L.; Cui, Z.; Hou, Z.; Li, Y. Synthesis and characterization of a NiCo2S4 2 S 4 and mesoporous carbon nanocomposite for energy storage. *Journal of Energy Storage* **2024**, *97*, 112873.
[30] Pervez, S.; Iqbal, M. Z. Capacitive and Diffusive Contributions in Supercapacitors and Batteries: A Critique of b-Value and the ν–ν1/2 Model. *Small* **2023**, *19* (48), 2305059.

Supplementary Files

This is a list of supplementary files associated with this preprint. Click to download.

- Graphicalabstract.pdf